THE EUROPEAN
PHYSICAL JOURNAL
APPLIED PHYSICS

Regular Article

Seeing oxygen disorder in YSZ/SrTiO₃ colossal ionic conductor heterostructures using EELS

T.J. Pennycook[1,2], M.P. Oxley[1,2], J. Garcia-Barriocanal[3], F.Y. Bruno[3], C. Leon[3], J. Santamaria[3], S.T. Pantelides[1,2], M. Varela[2,3], and S.J. Pennycook[1,2,a]

[1] Department of Physics and Astronomy, Vanderbilt University, Nashville, 37235 TN, USA
[2] Materials Science and Technology Division, Oak Ridge National Laboratory, P.O. Box 2008, Oak Ridge, 37831-6071 TN, USA
[3] Grupo de Fisica de Materiales Complejos, Universidad Complutense, 28040 Madrid, Spain

Abstract. Colossal ionic conductivity was recently discovered in YSZ/SrTiO₃ multilayers and was explained in terms of strain- and interface-enhanced disorder of the O sublattice. In the present paper we use a combination of scanning transmission electron microscopy and electron energy loss spectroscopy (EELS) and theoretical EELS simulations to confirm the presence of a disordered YSZ O sublattice in coherent YSZ/SrTiO₃ multilayers. O K-edge fine structure simulated for the strained disordered O sublattice phase of YSZ possesses blurred-out features compared to that of ordered cubic bulk YSZ, and experimental EELS fine structure taken from the strained YSZ of coherent YSZ/SrTiO₃ thin films is similarly blurred out. Elemental mapping is shown to be capable of resolving ordered YSZ O sublattices. Elemental mapping of O in the coherent YSZ/STO multilayers is presented in which the O sublattice is seen to be clearly resolved in the STO but blurred out in the YSZ, indicating it to be disordered. In addition, we present imaging and EELS results which show that strained regions exist at the incoherent interfaces of YSZ islands in STO with blurred out fine structure, suggesting these incoherent regions may also support high ionic conductivities. Recently, Cavallaro et al. reported electronic conductivities in samples of incoherent disconnected islands embedded in STO that are similar to the islands described herein. The presence of a region of O depleted STO at the interface with incoherent YSZ islands is revealed by EELS elemental mapping, implying the n-type doping of STO/YSZ nanocomposites with disconnected incoherent YSZ islands.

1 Introduction

Ionic conductivity is essential to the operation of fuel cells and sensors. In a H fuel cell, O and H are supplied separately to an anode and cathode that are separated by an electrically insulating electrolyte ionic conductor. Chemical reactions occur that release electrons at the anode and consume electrons at the cathode, resulting in an electric potential difference which can be tapped to provide power. The role of the ionic conductor is to permit either H or O ions, depending on the type of fuel cell, to travel between anode and cathode so that they may react to form H₂O. As the rate at which fuel is delivered is limited by the ionic conductivity of the electrolyte, so too is the current output of the fuel cell. In solid oxide fuel cells (SOFCs), O₂ is reduced to O ions at the cathode, which are transported though a solid oxide electrolyte to the anode, where they react with H to form water and electrons. SOFCs are among the most efficient types of fuel cells, but typically require very high operating temperatures in order for their electrolytes to achieve sufficient levels of ionic conductiv-

ity. The most commonly used O conducting electrolyte is yttria stabilized zirconia $(Y_2O_3)_x(ZrO_2)_{1-x}$ (YSZ). It typically reaches usable levels of ionic conductivity only at temperatures in excess of 700 °C [1–4]. Such high temperatures tend to reduce durability, increase costs, and generally limit their application. As a result, the search has been on for alternative O electrolytes with higher ionic conductivities at lower temperatures.

Although progress has been made towards the goal of higher O ionic conductivities at lower temperatures in bulk materials such as $Ce_{1-x}M_xO_{2-\delta}$ (M: Sm, Gd, Ca, Mn), the greatest enhancements have been achieved in heterogenous superlattices. Following work in CaF₂-BaF₂ multilayers [5,6], which showed an increase in the F ionic conductivity as the layer thickness was decreased, a variety of thin oxide heterostructures were fabricated. Enhancements of one to two orders of magnitude were achieved in (YSZ + 8.7 mol.% CaO)/Y₂O₃ [7] and YSZ/Y₂O₃ [8] multilayers and over three orders of magnitude in highly textured YSZ thin films grown on an MgO substrate [9]. In these multilayer materials, the conductivity increased as the film thicknesses were decreased or when the number of interfaces was increased, indicative of

a e-mail: pennycooksj@ornl.gov

Article published by EDP Sciences

an interfacial conduction pathway. It was proposed that in addition to space charge effects, the disordered and partially coherent interfaces of these multilayers enhanced the ionic conductivities by opening up pathways of decreased packing density [7,8]. On the other hand, segregation in disordered areas such as grain boundaries oriented perpendicular to the O ion current could also block O transport. The lack of such blocking grain boundaries was attributed to the extra order of magnitude enhancement of ionic conductivity in YSZ grown on MgO [9,10].

Far greater enhancements in O ionic conductivity were achieved by Garcia-Barriocanal et al. in YSZ/STO heterostructures [11]. The ionic conductivity of the 8 mol.% yttria YSZ in these heterostructures was measured to be up to eight orders of magnitude higher than bulk YSZ between room temperature and 600 K. The magnitude of the enhancement led to the effect being dubbed colossal ionic conductivity. The conductivity increased with the number of interfaces, but only slowly with the YSZ layer thickness up to 30 nm, suggesting that the majority of O conduction was occurring in the interface region.

STEM images and X-ray experiments revealed the YSZ/STO interfaces possessing colossal ionic conductivity to be coherent and atomically flat, with the YSZ rotating 45° around the c axis and expanding 7% in-plane such that the two cation sublattices fit together perfectly. Although small strains had been shown to enhance the diffusion of O ions in molecular dynamics simulations of YSZ [12], it was previously thought that disorder would provide the greater enhancement [7,8]. Strains as large as 7% had not, however, been considered. Based on lattice mismatch theory [13], one would not expect such large strains to be stable, yet Santamaria's group had produced coherent YSZ/STO interfaces despite the 7% mismatch. A coherent expansively strained material has the advantage of possessing a decreased packing density without the blocking effects of segregation or grain boundaries.

It is possible that a number of effects contribute to generate the observed colossal conductivity [6]. Arguments have been put forth interpreting the enhancement as an electronic effect [14], but the evidence supporting ionic enhancement is substantial [15]. An extensive theoretical analysis of ionic conduction and the possible origin of colossal conductivity, based on density functional theory (DFT) calculations, was recently reported by Pennycook et al. [16]. It was found that straining bulk zirconia 7% resulted in a completely different O sublattice, as illustrated in Figure 1. At temperatures between 1000 K and 2000 K the zirconia enters a phase in which the O sublattice is extremely disordered, to the point of appearing amorphous. At temperatures lower than 1000 K, the disorder quenches out, resulting in a phase in which the O atoms are ordered into zig-zags. However, simulating the full YSZ/STO multilayer with a 1 nm thick 8 mol.% yttria YSZ layer, it was found that the disordered O sublattice phase persisted in the YSZ to temperatures at least as low as 360 K as shown in Figure 2. The cation lattices remained coherent, but the STO and low temperature YSZ
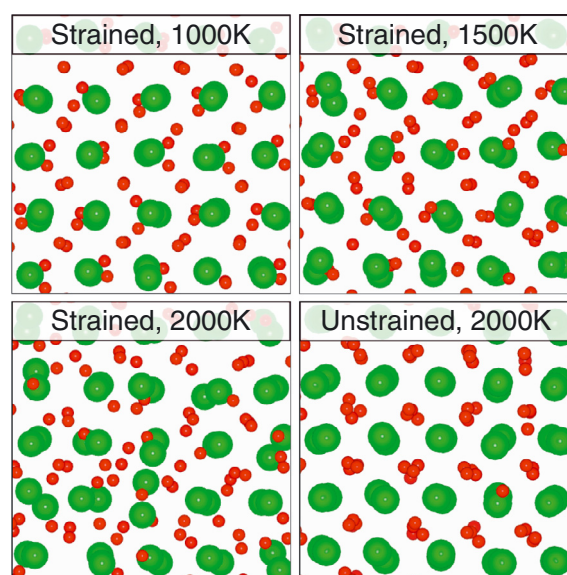

Fig. 1. (Color online) Zirconia structures resulting from quantum mechanical simulated annealing at various temperatures. O atoms are shown as small red spheres, and Zr atoms in green. The structures labeled as strained have been expanded 7% in the plane of the page. The zigzag ordering of the strained O sublattice shown at 1000 K persists down to 0 K, but breaks down at higher temperatures. At 2000 K and above the O positions appear random, in contrast to the unstrained material in which most O atoms simply oscillate about the cubic-fluorite positions. Reproduced from [16].
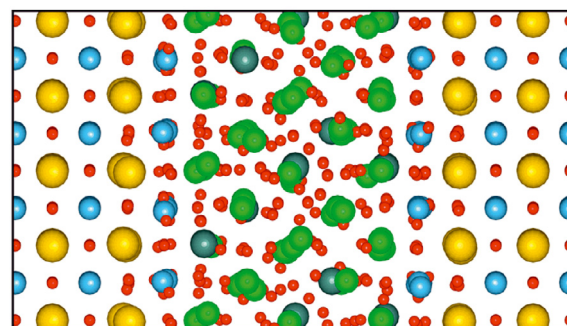

Fig. 2. (Color online) Structure of the 1 nm YSZ layer sandwiched between layers of STO at 360 K as determined by DFT MD calculations viewed down the ⟨100⟩ STO axis. Sr atoms are shown in yellow, Ti in blue, Zr in green, Y in gray, and O in red. The YSZ O sublattice disorder is comparable to that seen at 2000 K in the strained bulk. Reproduced from [16].

O sublattices are incommensurate, perturbing the weaker YSZ O sublattice into its disordered phase.

By monitoring the mean square displacements (MSD) of the O atoms as a function of time it was possible to extract diffusivities in the strained bulk ZrO_2 at a set of temperatures from 1000 K to 2500 K (see Fig. 3). An Arrhenius plot of the diffusivities produced an energy barrier of 0.4 ± 0.1 eV, close to the experimental 0.6 eV barrier reported for the colossal ionic conducting YSZ and far lower than the 1.1 eV unstrained bulk YSZ energy
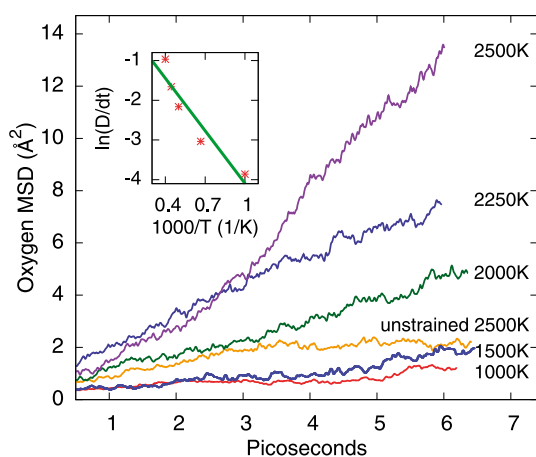
Fig. 3. (Color online) MSD of O atoms in strained and unstrained bulk ZrO_2 as a function of time during MD simulations at various temperatures. No significant net MSD occurred in the unstrained structure on this timescale for temperatures of 2000 K and below. Significant O MSD occurred in the unstrained structure only when the temperature was increased to 2500 K. The O in the strained structure is so much more mobile in the strained structure that its MSD at 1500 K is comparable to the unstrained 2500 K MSD after 6 ps. Inset: Arrhenius plot of D from the strained MSDs (same units). The linear fit shown in green yields an energy barrier of 0.4 ± 0.1 eV. Reproduced from [16].

barrier. The fact that the disordered O sublattice YSZ phase persists down to low temperatures in the multilayer allowed the results of the high temperature bulk diffusivity calculations to be applied to the YSZ of the multilayer at the low temperatures measured experimentally. Using the Nernst-Einstein relation, it was possible to estimate the ionic conductivity of the multilayer YSZ to be 4×10^6 higher than that of unstrained bulk YSZ at 500 K, comparable to the 8 orders of magnitude reported experimentally. The origin of colossal ionic conductivity therefore appears to be a combination of large expansive strain opening up the distance between cations, and the incompatibility of the YSZ and STO O sublattices perturbing the YSZ into the disordered O phase at low temperature.

In the present paper we report scanning transmission electron microscopy (STEM) and EELS results in combination with DFT and multislice EELS calculations which confirm the presence of a disordered YSZ O sublattice in coherent YSZ/STO colossal ionic conductor heterostructures. EELS spectra show the O K-edge fine structure from inside the YSZ of coherent YSZ/STO multilayers to be blurred out, in contrast to the sharp features seen in bulk YSZ. DFT simulations of the O K-edge fine structure using the $Z + 1$ approximation [17,18] confirm that the blurred out fine structure can be attributed to O sublattice disorder. In addition, we report atomic-resolution EELS elemental maps taken across the YSZ-STO interface, in which the O columns of STO are seen to blur out to the point of randomness in the strained YSZ. Multislice calculations confirm that this blurring out is what is expected in the disordered O sublattice phase of strained

YSZ. These results support the interpretation of strain and O sublattice disorder as the origin of colossal ionic conductivity in coherent YSZ/STO multilayers.

In addition we report imaging and EELS from incoherent YSZ/STO heterostructures in which the YSZ has formed islands rather than coherent thin films. We point out that these incoherent interfaces also contain expansively strained regions with disordered O atoms, and as such are also likely to support high O conductivities. EELS also provides evidence for the presence of a high concentration of vacancies in the STO surrounding incoherent YSZ islands, which would cause electronic conduction in such incoherent samples.

2 Methods

STEM and EELS measurements were performed on a Nion UltraSTEM operated at 100 kV using a cold field emission electron source, a corrector capable of neutralizing up to fifth order aberrations [19] and an Enfina EEL spectrometer. Some images were also obtained on a VG Microscopes HB501UX with a third order Nion aberration corrector (indicated in the figure caption). The YSZ/STO heterostructures were grown in a high oxygen pressure (3 mbar) pure O rf sputtering system and prepared in cross section or plan view geometry by conventional thinning, dimpling, and ion milling. The samples were tilted in the microscope to either the $\langle100\rangle$ or $\langle110\rangle$ cubic zone axis of STO. The principle component analysis (PCA) method of [20] was used to eliminate noise in atomic-resolution EELS elemental maps as described in [21].

EELS O K-edge fine structure simulations were performed using the $Z + 1$ approximation [17,18]. The calculations were carried out using DFT [22,23] in the generalized-gradient approximation and using the projector-augmented-wave method [24] with a plane-wave basis as implemented in the Vienna ab initio simulation package (VASP) code [25]. For faster convergence with respect to the k-point sampling density and greater accuracy, the linear tetrahedron method with Blöechl corrections was used for Brillouin zone integrations [26].

Image simulations were carried out using an absorptive multislice STEM code [27] with absorption due to thermal diffuse scattering included using an Einstein model [28]. The inelastic scattering coefficients for EELS were calculated using relativistically corrected Hartree Fock bound states and Hartree Slater continuum states [29]. An aberration free probe with a aperture semiangle of 30 mrad was assumed. Simulations were for a specimen thickness of approximately 110 Å with an EELS detector semiangle of 30 mrad. A Gaussian blur with a full width half maximum of 1 Å was applied to account for the finite source size.

3 Results and discussion

Due to the propensity of YSZ to facet, growing flat coherent YSZ/STO thin film multilayers is quite challenging.
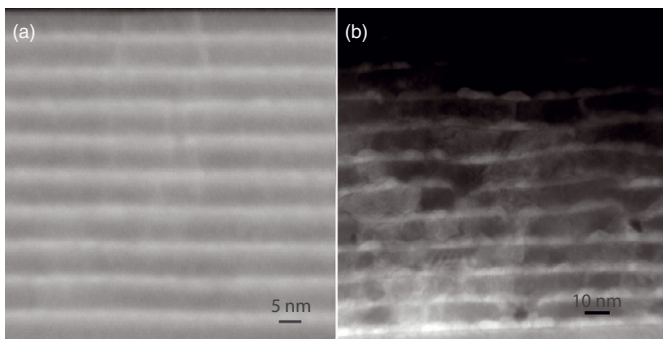
Fig. 4. Low magnification ADF images of YSZ/STO thin film multilayers acquired on a VG Microscopes HB501UX. (a) Sample showing flat coherent multilayers grown in 2007 (adapted from [11]). (b) Sample grown under slightly different growth conditions in 2009 showing incoherent layers.

Figure 4 shows low magnification annular dark field (ADF) images of two YSZ/STO samples, one grown in 2007 [11] and the other in 2009. Although both were grown using the same high pressure oxygen rf sputtering equipment under similar growth conditions, the layers in the 2007 sample are coherent and flat while those in the 2009 sample are not. Slight differences in the growth environment caused the YSZ in the 2009 sample to clump, facet, and bend. Dislocation cores formed at the interfaces, relieving the strain on the YSZ layers.

In an effort to recreate the coherent YSZ/STO multilayers grown in 2007, samples were grown with thinner nominal YSZ layer thicknesses. These samples often showed islanding, as shown in the high resolution ADF image shown in Figure 5, in which clumps of YSZ have formed surrounded on all sides by STO. They also possess coherent areas in which the YSZ is strained to match the STO, such as the area pointed to by the arrow in Figure 5a below the more obvious incoherent facet of the YSZ island. A similar island is shown in the high resolution ADF image shown in Figure 5b and in an ADF image (Fig. 5c) recorded simultaneously with a spectrum image of the area used to create the elemental map shown in Figure 5d. The elemental map shows the integrated intensities of the O K, Zr $M_{2,3}$ and $M_{4,5}$, and Ti $L_{2,3}$ edges as the red, green and blue channels of the image. Integration windows of approximately 50, 180, and 25 eV were used for the O, Zr, and Ti signals respectively. The only other features that should affect the signal in the large integration window used for Zr are the Y $M_{4,5}$ and $M_{2,3}$ edges, but this is fine as we are interested in distinguishing YSZ from STO. Red and blue make purple while red and green make yellow, so STO will appear purple and YSZ yellow. The island is clearly zirconia.

Figure 6 shows coherent interfaces looking down the $\langle 100 \rangle$ and $\langle 110 \rangle$ axes of the STO. As the YSZ must rotate 45° to fit the STO cation lattice, these correspond to the $\langle 110 \rangle$ and $\langle 100 \rangle$ axes of the YSZ respectively. Intensity in ADF imaging varies roughly as the square of the atomic number of elements being imaged. With atomic numbers 38, 39 and 40, respectively, Sr, Y and Zr are neighbors
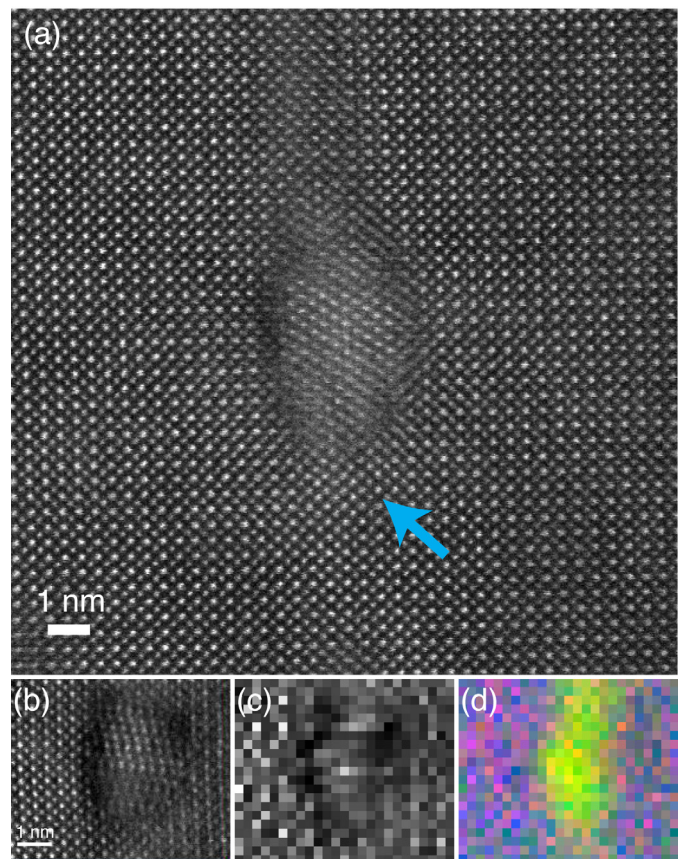

Fig. 5. (Color online) High resolution ADF images of islands of YSZ in STO are shown in (a) and (b). The arrow in (a) points to a section of coherent YSZ/STO. An elemental map created from a spectrum image of the the area imaged in (b) is shown alongside a simultaneously acquired ADF image (c) in (d). Red, green and blue channels of (d) are composed of the integrated intensities of the O K, Zr $M_{2,3}$ and $M_{4,5}$, and Ti $L_{2,3}$ edges respectively, causing STO to appear purple and YSZ yellow. (b), (c) and (d) reproduced from [30].

on the periodic table and will therefore appear similarly bright compared to Ti with atomic number 22. Against the background of these heavier atoms, the O columns are not readily discernible. STO therefore appears with equal numbers of bright and dark columns, while the YSZ columns all appear bright. Linetraces taken in the $\langle 110 \rangle$ directions of the images in Figure 6 show a series of bright columns surrounded by the alternating bright and dark columns, identifying the YSZ and STO. The areas of the images used in the linescans are delineated in the figure with red rectangles. Arrows mark the transitions between the alternating bright and dark columns of STO and the more consistently bright columns of the YSZ in the linescans and the corresponding points in the images. The width of the transition from YSZ to STO contrast is roughly one unit cell, consistent with the expected beam broadening for this sample thickness.

Figure 7a shows another section of coherent YSZ/STO layers. A spectrum image (SI) was acquired, consisting of EEL spectra taken in a 4×24 pixel grid within the area
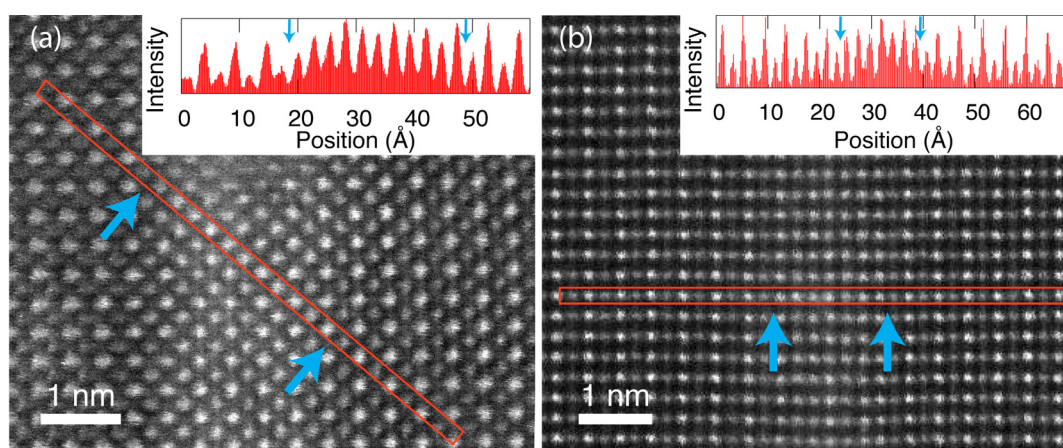
Fig. 6. (Color online) High resolution ADF images of sections of coherent regions of YSZ/STO multilayers looking down the STO $\langle 100 \rangle$ and YSZ $\langle 110 \rangle$ directions in (a) and the STO $\langle 110 \rangle$ and YSZ $\langle 100 \rangle$ directions in (b). ADF intensity is plotted as a function of position along the long direction of the red boxes for both images in the insets. The intensity is integrated along the direction of the short side of the red boxes. Blue arrows indicate the transition from consistently high intensity peaks to alternating bright dark peaks in the linetraces, corresponding to the transition from YSZ to STO. The corresponding positions on the images are also marked with arrows. (a) is adapted from [30].
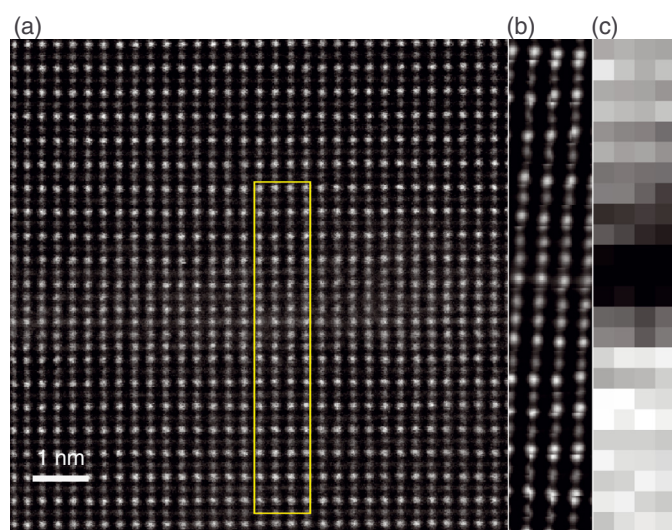

Fig. 7. (Color online) (a) High resolution ADF image of a $\langle 100 \rangle$ YSZ layer sandwiched between $\langle 110 \rangle$ STO layers. A SI was acquired from the area indicated by the yellow rectangle superimposed on (a). An ADF image recorded simultaneously with the SI is shown in (b) at the same scale as the Ti elemental map shown in (c). A drop in the Ti intensity correlates with the more consistently bright columns of the YSZ layer.

shown in the yellow rectangle. An exposure time of 2 s was used for each pixel. During the acquisition of each pixel of the SI, the beam was scanned in a 16×16 pixel subgrid, allowing an ADF image (Fig. 7b) to be recorded at higher spatial resolution simultaneously with the EELS SI. As sample drift almost always occurs during the long periods of time needed to record SIs, the higher resolution simultaneously recorded ADF image is useful in identifying exactly where the spectra were recorded. From Figure 7b

it is clear that there was some sample drift down and to the left, but the STO is clearly discerned from the YSZ by its alternating bright and dark columns. A map of the Ti concentration created from the integrated background subtracted Ti L-edge is shown in Figure 7c at the same scale as the simultaneously recorded ADF. In the STO, bright rows are seen in the Ti map where darker Ti columns are seen in the ADF image. Near the interface, the Ti intensity begins to drop. Moving into the layer of more consistently bright atoms, the Ti intensity continues to decrease, supporting the identification of the layer as YSZ.

EELS fine structure reflects the local bonding environment. Changes in either bond-lengths or coordination shift or change the intensities of the fine structure features. In a disordered material, with many slightly different local bonding environments, the EELS spectrum is the sum of many slightly different fine structure features. One, therefore, expects the fine structure features of a disordered material to be blurred out in comparison to an ordered material. We illustrate this effect with DFT $Z+1$ O K-edge fine structure simulations for ordered cubic ZrO_2 and disordered O sublattice strained ZrO_2. For the ordered structure it is only necessary to calculate the $Z+1$ projected density of states for a single O site, as all the O sites are equivalent. To simulate the fine structure of the disordered material we summed the $Z+1$ projected density of states calculated for 6 different O atoms in the high temperature disordered O sublattice strained bulk structure produced by the MD calculations of reference [16]. Monkhorst-Pack k-point meshes of up to $18 \times 18 \times 18$ were used for the small ordered supercell and up to $4 \times 4 \times 4$ for the much larger disordered O sublattice structure. The resulting spectra were convolved with a 0.5 eV full width half maximum Gaussian to facilitate comparison to experiment. The results are shown in Figure 8 normalized
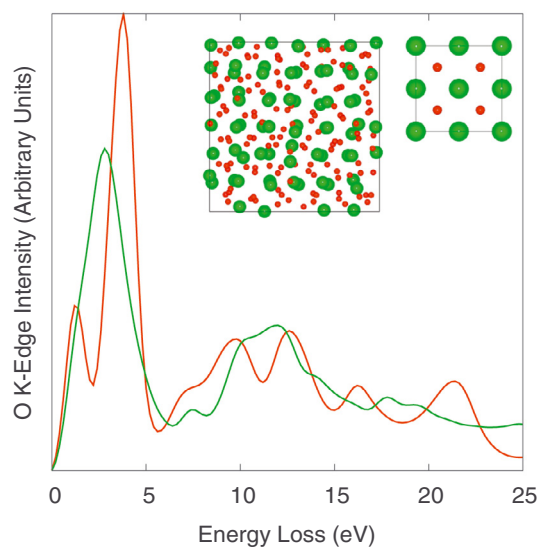
Fig. 8. (Color online) EELS O K-edge fine structure simulated using DFT and the $Z+1$ approximation for bulk ordered cubic ZrO_2 (shown in red) and the 2000 K strained bulk structure with the extremely disordered O sublattice (shown in green). The energy loss is taken to be zero at the Fermi energy. Both spectra were normalized to the intensities integrated over the first 50 eV and broadened with a 0.5 eV Gaussian. It is seen that the disorder causes the fine structure to blur out.

Fig. 9. (Color online) (a) O K-edge fine structure from the thin YSZ layer shown in Figure 7 plotted in green and from bulk cubic YSZ in red. The multilayer spectrum was created from the same spectrum image used to produce the Ti map in Figure 7. Pixels were summed up in the area corresponding to the green box superimposed on the simultaneous ADF image shown in (b).

to the integrated intensity of the first 50 eV of the edges. The simulated fine structure features of the ordered structure correspond well to those seen in normal bulk YSZ. Shifts in the features of the projected density of states for each of the different $Z + 1$ sites used in the simulation for the disordered structure sum up to create a fine structure which appears much like a blurred version of the fine structure of the ordered structure. Where there are two peaks close together in the fine structure of the ordered material, there is a single broad peak for the disordered material.

In Figure 9a the YSZ O K-edge fine structure obtained from the spectrum image of the coherent region of the STO/YSZ multilayer shown in Figure 7 is compared to that obtained from bulk YSZ. From the simultaneously acquired ADF image it is easy to pick out which SI pixels are inside the YSZ layer. The spectrum shown in green in Figure 9a was created by summing over the 20 SI pixels corresponding to the area within the green box superimposed on the simultaneously acquired ADF image shown in Figure 9b. With a per pixel exposure time of 2 s, this corresponds to a 40 s exposure, plenty of time for fine structure to dominate the noise, yet only broad peaks are seen. Compared to the spectrum from bulk YSZ, the multilayer spectrum appears blurred out just as predicted by theory for a structure with O disorder. It is likely there is some contribution to the multilayer spectrum from STO – the integrated $TiL_{2,3}$ signal does not go to zero in the YSZ layer – but the spectrum does not appear to be a simple linear combination of YSZ and STO bulk fine structure. STO has a prominent prepeak at very nearly the same energy as bulk YSZ, yet the multilayer YSZ spectrum has
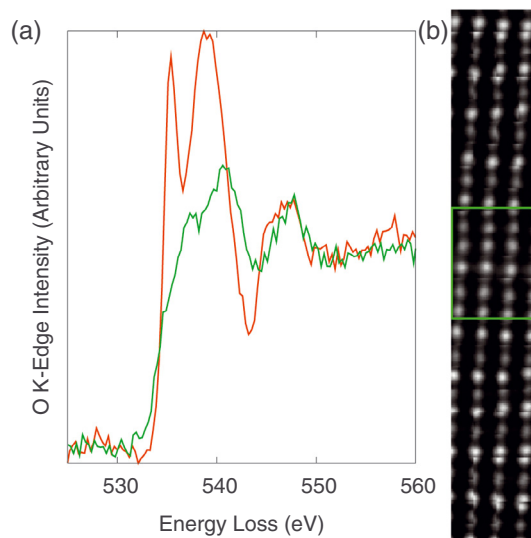
only a weak strength in this region, supporting the view that the fine structure is blurred out due to O disorder in the YSZ.

Another way EELS can be used to search for disorder is through atomic-resolution elemental mapping. Images created from the integrated edge intensities of each pixel of spectrum images are capable of independently resolving the structure of each element's sublattice, provided they all have well defined edges which do not overlap. In order to reduce the effects of sample drift and achieve the highest spatial resolution, spectrum images used for atomic-resolution elemental mapping tend to have larger number of pixels and shorter per pixel exposure times than spectrum images used to study fine structure.

Maximizing sample stability is vital to successful high spatial resolution elemental mapping. Modern instruments such as the UltraSTEM take stability to a new level, and elemental maps taken on it achieve resolutions sufficient to resolve even fine features such as Jahn-Teller distortions. When viewed down the $\langle 110 \rangle$ direction, the pure O columns of STO are separated by 2.76 Å in plane and are routinely resolved using elemental mapping. If YSZ is coherently strained to match the STO and the O atoms were ordered as in bulk YSZ, they would also have a separation of 2.76 Å as illustrated in Figure 10a. As viewed in the model, the material is oriented such that the STO is viewed down the $\langle 110 \rangle$ and the YSZ down the $\langle 100 \rangle$ axis. The structure is the result of DFT calculations which optimized the size of the supercell in the direction perpendicular to the interface. The O spacing in this direction is a slightly shorter 2.39 Å. Both of these lengths are greater than the resolution typically achieved in EELS
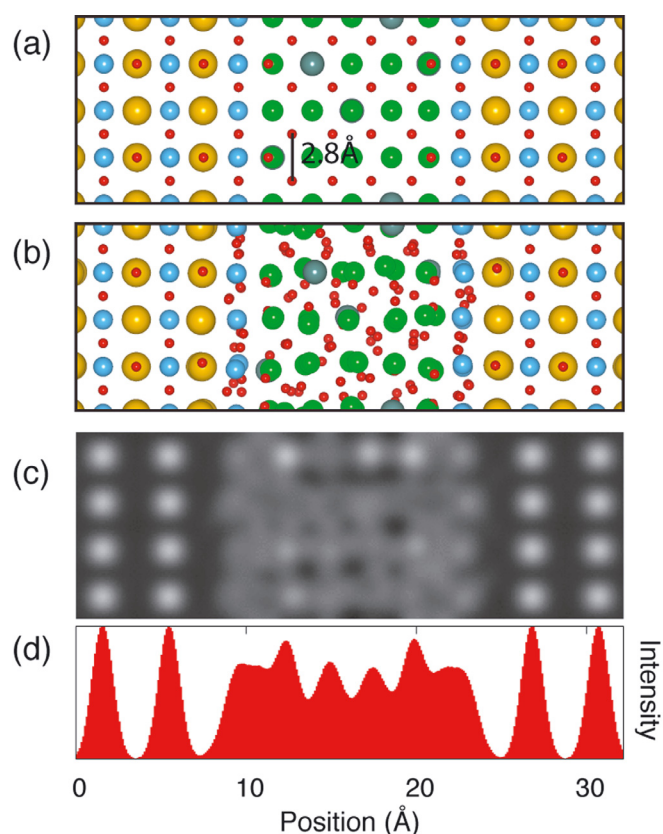
Fig. 10. (Color online) (a) Model of YSZ/STO multilayer with ordered strained YSZ O sublattice viewed such that the STO is seen down the $\langle 110 \rangle$ axis. In this orientation the pure O columns of STO can be resolved using high spatial resolution elemental mapping. The O columns of the strained ordered YSZ have the same 2.76 Å in plane separation as the pure O columns in STO in the vertical direction of the figure and a slightly shorter 2.39 Å in the horizontal direction. As such, the YSZ O columns should be resolved in an elemental map, if the O atoms are ordered. If they are instead disordered as in (b), then one would expect to see a highly blurred out structure or just a blur. The blurring out is illustrated in (c) with a multi-slice simulation of the O K-edge elemental map of the structure shown in (b), viewed in the same orientation. The integrated intensity of each column of pixels in the simulated elemental map is shown in (d). The intensity is shown in arbitrary units.

maps acquired on the UltraSTEM. Therefore, if the O lattice is ordered it should be resolved.

Figure 10b is the result of performing simulated annealing with DFT on the structure shown in Figure 10a. The O sublattice disorders to the point of randomness, as in the high temperature MD of bulk strained YSZ. A multislice simulation of the O K-edge elemental map that would result from viewing a sample consisting of the 11 Å thick structure shown in Figure 10b repeated to a thickness of approximately 110 Å is shown in Figure 10c. The O columns are clearly resolved in the STO but appear quite blurred out in the interfacial planes of TiO₂ and in the YSZ. The repetition of the relatively thin supercell used in the DFT calculation to make a thicker sample im-
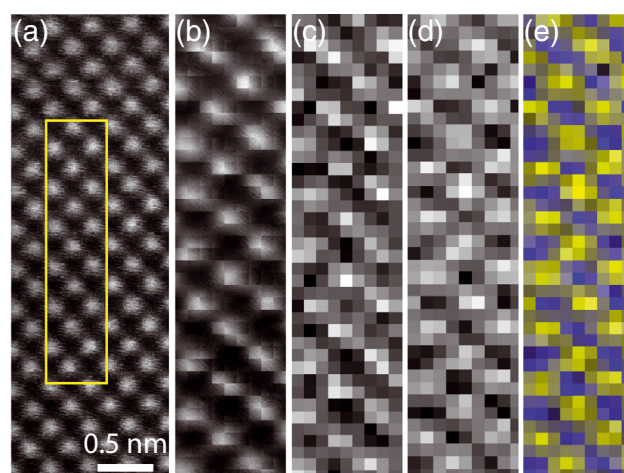

Fig. 11. (Color online) (a) High resolution ADF image of bulk YSZ viewed down the $\langle 100 \rangle$ axis. A SI was acquired from the area indicated with the yellow box simultaneously with the ADF image shown in (b). The Zr $M_{4,5}$ and O K-edge integrated intensities of the PCA processed SI are shown as a function of position in (c) and (d) respectively. A composite of the two in which the red and green channels are composed of the O map (making O intensity appear yellow) and the blue channel of the Zr map is shown in (e).

poses order that is not likely to exist in a real sample. In a real sample, O atoms will be distributed over far more probe positions, causing even greater spatial blurring than in the simulation. If the YSZ O sublattice is disordered, an O elemental map should resolve columns in the STO but only a blur in the YSZ.

To demonstrate that ordered O atoms in YSZ are resolved when viewed down the $\langle 100 \rangle$ axis, we have performed atomic-resolution elemental mapping in bulk YSZ. A high resolution ADF image of bulk YSZ is shown in Figure 11a. A yellow box delineates the region nominally used for the spectrum image. An ADF image recorded simultaneously with the spectrum image is shown in Figure 11b, from which it is clear what the true positions of the heavy columns were during EELS acquisition. The SI data were denoised using PCA, and the integrated intensities of the Zr M and O K-edges shown in Figures 11c and 11d respectively. A composite of the two maps is shown in Figure 11e in which the blue channel is composed of the Zr map and the red and green channels composed of the O map. As such, Zr columns appear blue and O columns appear yellow. Areas with high intensity in the simultaneous ADF image correspond to Zr sites, and also appear bright in the Zr elemental map. The O map also shows a lattice of bright spots. They are between the Zr columns seen in the ADF as is the correct position of the O atoms in the ordered material.

Having established that an ordered YSZ O sublattice should be resolved, we now turn to elemental maps of the YSZ/STO multilayers. PCA processed Ti and O elemental maps taken from the boxed area in Figure 12a are shown in Figures 12c and 12d and as a composite in which O is
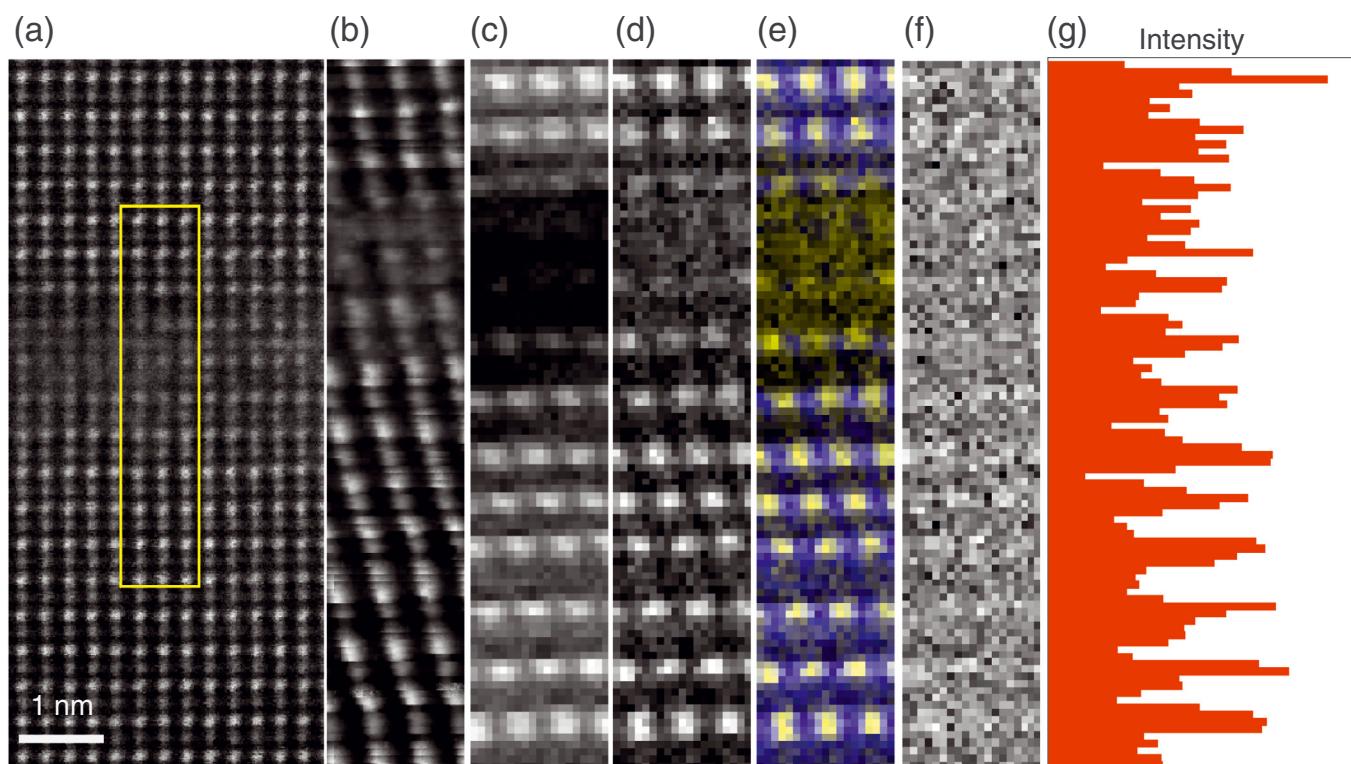
Fig. 12. (Color online) (a) High resolution ADF image of a section of coherent YSZ/STO multilayers viewed down the ⟨110⟩ STO axis. An ADF image recorded simultaneously with a SI taken in the area indicated by the yellow box is shown in (b). Integrated Ti L and O K-edge intensity elemental maps extracted from the PCA processed SI are shown in (c) and (d) and as a composite map in (e) in which O intensity is shown in yellow and Ti intensity is shown in blue. An O elemental map extracted from the SI without PCA processing is shown in (f), and the integrated intensity of each row of pixels in the raw O map is shown in (g). The intensity is given in arbitrary units, with the background subtracted to improve the contrast.

shown in yellow and Ti in blue in Figure 12e. In addition an O map produced from the SI without PCA processing is shown in Figure 12f and the integrated intensity of each row of pixels in the raw O map is plotted at the same scale beside it in Figure 12g. From the simultaneous ADF image, in Figure 12b, it is clear that there was some sample drift over the course of the 6 min and 27 s it took to acquire the 19×98 pixel SI. The drift is seen to be relatively uniform and without any large jumps. More importantly the Ti and pure O columns are clearly resolved in the STO in the elemental maps and in the correct positions based on the positions of the Sr and Ti columns in the simultaneous ADF image. In the YSZ region of the O maps, the O lattice blurs out and all but disappears, consistent with the presence of a disordered YSZ O sublattice.

The ADF images show small variations of intensity between the rows of atoms inside the YSZ region consistent with the patterning of the surrounding STO, but with much lower contrast, suggesting there is some STO above or below the YSZ. The Ti map shows only very weak intensity columns in the YSZ region. Their presence is significant, however, as the only O columns that appear in the YSZ region in the O elemental maps are similarly weak, and positioned vertically aligned and horizontally interspersed with the dim Ti columns. As can be seen from the model in Figure 10a, the spacing between rows

of pure O columns in STO is twice that of ordered YSZ. If the YSZ O atoms were ordered as in the model, we would therefore expect to see strong peaks at twice the frequency as in STO, not just weak spots in TiO rows against a relatively uniform background. The lack of such peaks thus strongly suggests that we are indeed seeing O disorder in the YSZ.

Further support for the presence of a disordered YSZ O sublattice is seen by comparing the linetraces of the experimental and theoretical O elemental maps. The average intensity of each row of pixels in the raw O map shows clear contrast in the STO with peaks corresponding to the TiO_2 planes, but very little contrast in the YSZ region. This lack of contrast is similar to that seen in Figure 10d for the O elemental map simulated for the multilayer structure with extreme O disorder produced by DFT calculations. We note that the blurring out of the heavy ions in the YSZ region seen in the ADF images is consistent with the deviations seen in the Zr positions seen in the simulated multilayer shown in Figure 10b. Although the Zr atoms are not disordered to the extreme degree of the O atoms, they do not form perfect columns, which would cause some blurring out of the Zr columns in the ADF images.

In addition to the coherent STO/YSZ interfaces we also see evidence for a combination of strain and O
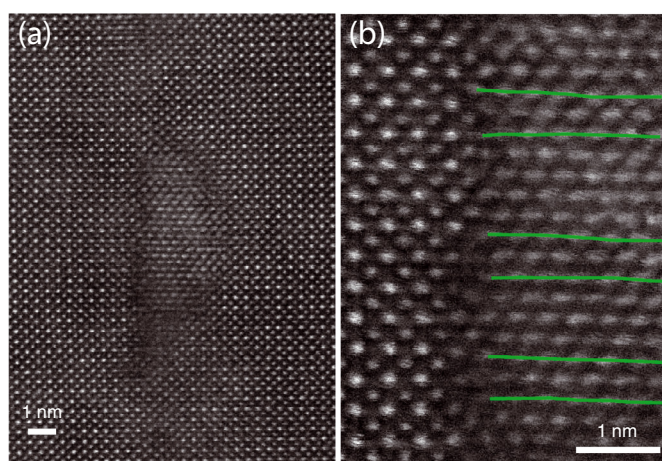
Fig. 13. (Color online) (a) High resolution ADF image of an incoherent YSZ island surrounded by STO. (b) A magnified view of the interface on the left side of the island shown in (a). The green lines are drawn through the centers of the Zr columns, illustrating the expansive strain that occurs in these regions near the interface. Adapted from [30].

disorder at the interfaces of incoherent YSZ islands and the surrounding STO. Figure 13 shows a high resolution ADF image of a YSZ island. Strain and disorder are associated with dislocation cores such as those seen in the magnified view of Figure 13. Areas of YSZ expansion and contraction appear along the interface. The green lines follow the YSZ unit cells from the middle of the island to the interface where the unit cells are expanded. The lattice spacing around the dislocation cores is up to $10 \pm 2\%$ larger than in the center of the island. This strain is even greater than the 7% of YSZ coherently layered with STO, suggesting the region may also support a high O conductivity.

A similar island is shown in the ADF image in Figure 14a for which a 9×55 pixel spectrum image was recorded in the area indicated by the yellow rectangle with a 0.3 s per pixel exposure time. The O K-edge extracted from spectra integrated over equal numbers of pixels in the STO, the middle of the YSZ island and from the interface region are shown background subtracted in Figure 14e. The regions used for the integration are indicated by boxes superimposed on the simultaneous ADF image. The O-edge from the center of the YSZ island, which is not strained, looks very much like that of normal bulk YSZ. The fine structure of the edge from the interface regions shows only broad features, however, other than features on the scale of noise. Integrating over the interfacial region, one would expect to see a combination of STO and YSZ fine structure features, yet in these interfacial regions the fine structure does not appear to be a simple linear combination of the two. The blurred out appearance of the fine structure at the interface is again suggestive of O disorder. As the combination of expansive strain and O sublattice disorder enhances the O ionic conductivity, it is likely that these strained interfacial regions can also support enhanced ionic conductivities. Blocking effects may

prevent them from achieving such high ionic conductivities as reported for the coherent YSZ/STO multilayers. In addition, incoherent islands of YSZ in STO are unlikely to be well connected, meaning that although AC conductivity measurements could show high conductivities due to ionic conductivity in isolated expansively strained regions, O transport over long distances may not be possible.

The integrated Ti and O-edge intensities are shown in parts (c) and (d) of Figure 14 alongside the simultaneously acquired ADF image shown at the same scale. The Ti signal intensity drops off quickly at the interface with the YSZ island where it is dark. The O signal is bright in both the STO and the YSZ but is significantly reduced around the interface region. The reduced O signal suggests the presence of an enhanced vacancy concentration at the interface. The O deficient region extends into the STO. O deficiency at dislocation cores in STO and related structures and its effect on current transport has been reported previously [31,32]. Vacancies cause STO to become metallic.

Experiments on samples of STO containing YSZ islands have been reported by Cavallaro et al. [33], which they believe show the majority of the conduction occurring in samples they have grown by pulsed laser deposition to be electronic in nature. They report a one order of magnitude decrease in the conductance of their material as they decrease the O partial pressure from 1 bar pure oxygen to 3×10^{-4} bar. The decrease in partial pressure should increase the number of O vacancies in the material. The decrease in conductance with partial O pressure they measure could therefore be explained, as they suggest, by the n-type doping of vacancies compensating an intrinsic p-type doping of the material. p-type doping could, for instance, be caused by diffusion of Y into the STO.

Clearly the nature of the conductivity of STO/YSZ nanocomposites depends on the balance of doping by interdiffusion of ions and the concentration of vacancies in the STO. We note that DFT calculations suggest that it is energetically unfavorable for O vacancies to leak out of YSZ into the STO when they are grown in coherent multilayers [16]. Additionally, the conductivity of the coherent STO/YSZ multilayers grown by Garcia-Barriocanal et al. showed negligible dependence on the partial oxygen pressure [11]. These facts support ionic conductivity as the dominate form of the conductivity observed in the coherent YSZ/STO produced by Garcia-Barriocanal et al. If electronic conduction was dominant, the change in the STO vacancy concentration introduced by changing the O partial pressure should have significantly altered the conductivity.

4 Conclusions

Evidence has been presented supporting the presence of O disorder in the YSZ of coherent YSZ/STO heterostructures in line with the predictions of DFT simulations that attributed the origin of colossal ionic conductivity to the presence of a disordered O sublattice phase of YSZ. DFT $Z + 1$ approximation simulations of the O K-edge fine
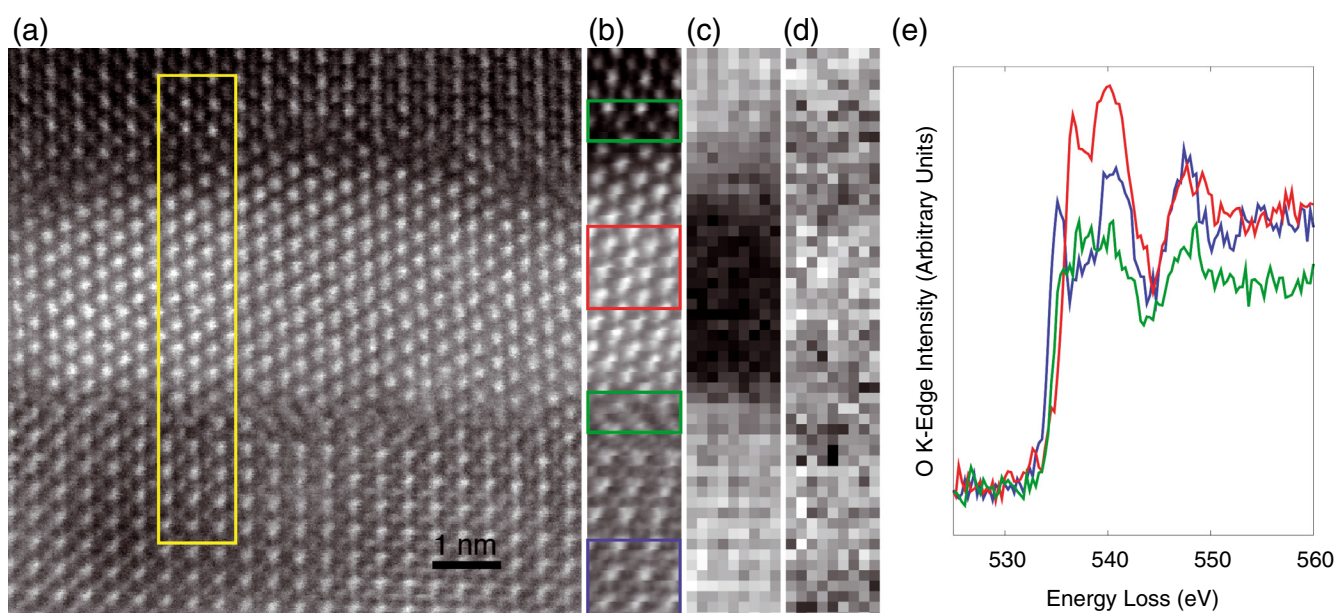
Fig. 14. (Color online) (a) High resolution ADF image of an incoherent island of YSZ surrounded by STO. (b) ADF image recorded simultaneously with a SI recorded in the area indicated by the yellow box in (a). Ti and O elemental maps extracted from the SI are shown in (c) and (d) at the same scale as (b). The O K-edge extracted from the regions indicated by the corresponding colors in (b) are shown in (e). The green spectrum shows a significant reduction in the continuum region of the spectrum, indicating the presence of O vacancies.

structure features of the disordered O sublattice phase of strained YSZ appear to be blurred out versions of the fine structure observed in ordered bulk YSZ. EELS experiments confirm that the O K-edge fine structure of coherent YSZ/STO interfaces is in fact blurred out compared to that of bulk YSZ. EELS elemental mapping was shown to be capable of seeing individual O columns in bulk cubic YSZ. The fact that EELS elemental mapping of coherent regions of YSZ/STO multilayers show clear O columns in the STO, but essentially only a blur in the YSZ, is strong evidence for the presence of O disorder in the strained multilayer YSZ. In addition, we have shown that strained regions exist around dislocation cores at the interface of YSZ islands surrounded by STO, and that the O K-edge from these regions is also blurred out as if the O sublattice is disordered, suggesting that these regions may also be capable of high ionic conductivity. The incoherent STO/YSZ interfaces show high concentrations of O vacancies, which are likely to cause electronic conductivity in such samples.

References

1. B.C.H. Steele, A. Heinzel, Nature **414**, 345 (2001)
2. R.M. Ormerod, Chem. Soc. Rev. **32**, 17 (2002)
3. J.B. Goodenough, Ann. Rev. Mater. Res. **33**, 91 (2003)
4. J.A. Kilner, Nat. Mater. **7**, 838 (2008)
5. J. Maier, Solid State Ion. **131**, 13 (2000)
6. N. Sata, K. Eberman, K. Eberl, J. Maier, Nature **408**, 946 (2000)
7. A. Peters, C. Korte, D. Hesse, N. Zakharov, J. Janek, Solid State Ion. **178**, 67 (2007)
8. C. Korte, A. Peters, J. Janek, D. Hesse, N. Zakharov, Phys. Chem. Chem. Phys. **10**, 4623 (2008)
9. I. Kosacki, C.M. Rouleau, P.F. Becher, J. Bentley, D.H. Lowndes, Solid State Ion. **176**, 1319 (2005)
10. C.A.J. Fisher, H. Matsubara, J. Eur. Ceram. Soc. **19**, 703 (1999)
11. J. Garcia-Barriocanal, A. Rivera-Calzada, M. Varela, Z. Sefrioui, E. Iborra, C. Leon, S.J. Pennycook, J. Santamaria, Science **321**, 676 (2008)
12. K. Suzuki, M. Kubo, Y. Oumi, R. Miura, H. Takaba, A. Fahmi, A. Chatterjee, K. Teraishi, A. Miyamoto, Appl. Phys. Lett. **73**, 1502 (1998)
13. J.W. Matthews, A.E. Blakeslee, J. Cryst. Growth **27**, 118 (1974)
14. X. Guo, Science **324**, 465 (2009)
15. J. Garcia-Barriocanal, A. Rivera-Calzada, M. Varela, Z. Sefrioui, E. Iborra, C. Leon, S. Pennycook, J. Santamaria, Science **324**, 465 (2009)

16. T.J. Pennycook, M.J. Beck, K. Varga, M. Varela, S.J. Pennycook, S.T. Pantelides, Phys. Rev. Lett. **104**, 115901 (2010)

17. R. Buczko, G. Duscher, S.J. Pennycook, S.J. Pantelides, Phys. Rev. Lett. **85**, 2168 (2000)

18. W. Luo, M. Varela, J. Tao, S.J. Pennycook, S.T. Pantelides, Phys. Rev. B **79**, 052405 (2009)

19. O.L. Krivanek, G.J. Corbin, N. Dellby, B.F. Elston, R.J. Keyse, M.F. Murfitt, C.S. Own, Z.S. Szilagyi, J.W. Woodruff, Ultramicroscopy **108**, 179 (2008)

20. M. Bosman, M. Watanabe, D.T.L. Alexander, V.J. Keast, Ultramicroscopy **106**, 1024 (2006)

21. M. Varela, M.P. Oxley, W. Luo, J. Tao, M. Watanabe, A.R. Lupini, S.T. Pantelides, S.J. Pennycook, Phys. Rev. B **79**, 085117 (2009)

22. P. Hohenberg, W. Kohn, Phys. Rev. **136**, 864 (1964)

23. W. Kohn, L.J. Sham, Phys. Rev. **140**, A1133 (1965)

24. P.E. Blöchl, Phys. Rev. B **50**, 17953 (1994)

25. G. Kresse, J. Furthmuller, Phys. Rev. B **54**, 11169 (1996)

26. P.E. Blöchl, O. Jepsen, O.K. Andersen, Phys. Rev. B **49**, 16223 (1994)

27. L.J. Allen, S.D. Findlay, M.P. Oxley, C.J. Rossouw, Ultramicroscopy **96**, 47 (2003)

28. L.J. Allen, C.J. Rossouw, Phys. Rev. B **42**, 11644 (1990)

29. M.P. Oxley, L.J. Allen, Phys. Rev. B **57**, 3273 (1998)

30. T.J. Pennycook, M. Varela, M.J. Beck, J. Garcia-Barriocanal, F.Y. Bruno, C. Leon, J. Santamaria, S.T. Pantelides, S.J. Pennycook, Microsc. Microanal. **16**, 100 (2010)

31. M. Kim, G. Duscher, N.D. Browning, K. Sohlberg, S.T. Pantelides, S.J. Pennycook, Phys. Rev. Lett. **86**, 4056 (2001)

32. R.F. Klie, J.P. Buban, M. Varela, A. Franceschetti, C. Jooss, Y. Zhu, N.D. Browning, S.T. Pantelides, S.J. Pennycook, Nature **435**, 475 (2005)

33. A. Cavallaro et al., Solid State Ion. **181**, 592 (2010)

To access this journal online:
www.edpsciences.org